Applied Catalysis B: Environmental 312 (2022) 121405

Contents lists available at ScienceDirect

Applied Catalysis B: Environmental

journal homepage: www.elsevier.com/locate/apcatb

Porous titania nanotube confined ultrafine platinum catalysts synthesized by atomic layer deposition with enhanced hydrolytic dehydrogenation performance

Jiankang Zhang [a,*], Wenlong Yu [b], Dan Feng [c], Hao Xu [a,d], Yong Qin [a,e]

[a] Interdisciplinary Research Center of Biology & Catalysis, School of Life Sciences, Northwestern Polytechnical University, Xi'an 710072, PR China
[b] State Key Laboratory Base of Eco-Chemical Engineering, College of Chemical Engineering, Qingdao University of Science and Technology, Qingdao 266042, PR China
[c] Analytical & Testing Center, Northwestern Polytechnical University, Xi'an 710072, PR China
[d] School of Chemistry and Chemical Engineering, Northwestern Polytechnical University, Xi'an 710072, PR China
[e] State Key Laboratory of Coal Conversion, Institute of Coal Chemistry, Chinese Academy of Sciences, Taiyuan 030001, PR China

ARTICLE INFO

Keywords:
Atomic layer deposition
Confined catalysts
Porous TiO_2 nanotubes
Ammonia borane
Hydrolytic dehydrogenation

ABSTRACT

Synthesizing the catalysts with high activity and stability has always been the research hotspot in the field of heterogeneous catalysis, and the confinement provides a promising route to achieve the goal. Herein we report the porous TiO_2 nanotube confined Pt catalysts synthesized by the template-assisted atomic layer deposition (ALD) strategy for hydrolytic dehydrogenation of NH_3BH_3, in which the ultrafine Pt nanoparticles are decorated on the inner surfaces of the nanotubes with increased Pt-TiO_2 interfacial sites compared with the supported Pt/TiO_2 counterparts. Combined with the porous structures of the nanotubes with suitable thickness and large open ends, these factors synergistically contribute to the excellent catalytic performances of the confined Pt@TiO_2 catalysts. The present strategy can be extended to prepare the corresponding PtNi@TiO_2 bicomponent catalysts exhibiting the further boosted activity with a TOF value of 1055.2 mol_{H2} mol_{Pt}^{-1} min^{-1}. This work offers a reliable and general approach for synthesizing the confined catalysts with high efficiency.

1. Introduction

Design and synthesis of catalysts with high activity, selectivity and stability are the primary goal for the catalytic researchers [1–3]. Confinement catalysis is a significant route to regulating the catalytic performances, and the corresponding confined catalysts, generally exhibiting unique catalytic performance due to the confinement effect, have been drawn increasing attention in recent decades [3–27]. Anchoring metal nanoparticles inside the nanospaces of the porous supports such as silica, zeolites, metal-organic frameworks and carbon sphere nanoreactors can realize the precise modulation toward the size of metal nanoparticles, inhibit their sintering/leaching and even modify their electronic properties [3–29], which is a widely applied strategy to modulate the catalytic performances. However, the relatively smaller entrance size (generally < 2 nm) to the inner active metal nanoparticles confined in the porous materials may lower the reaction rates or limit the substrate-scope due to the potential diffusion limitations [28,29].

Nanotube confined catalysts generally possess large diameters (open ends) and the reactants can facilely access the confined metal nanoparticles. Especially, the research results from Bao's and Li's group demonstrate that carbon nanotube (CNT) confined catalysts exhibit excellent catalytic performance compared with the supported counterparts due to the unique confinement effects of CNTs, which also present remarkably improved stability by inhibiting the sintering/leaching of metal nanoparticles [30–33]. Besides the CNT confined catalysts, a series of oxide nanotube confined catalysts such as Pt@TiO_2 [34], Ni@TiO_2 [35] and copper-phyllosilicate nanotube confined Cu@CuPSNT [36,37] catalysts have also been reported and outstanding catalytic performance was obtained. It should be noted that the degree of confinement toward metal nanoparticles is difficult to achieve 100% for the catalysts synthesized by the traditional methods such as ion exchange and wet impregnation, i.e., a certain number of metal nanoparticles are inevitably anchored on the outer surfaces of the supports, which hinders the precise establishment of the structure-performance relationships of the catalysts. Therefore, a facile and reliable approach that can realize the precise construction of confined catalysts with

* Corresponding author.
E-mail address: zhangjiankang@nwpu.edu.cn (J. Zhang).

https://doi.org/10.1016/j.apcatb.2022.121405
Received 29 January 2022; Received in revised form 30 March 2022; Accepted 9 April 2022
Available online 16 April 2022

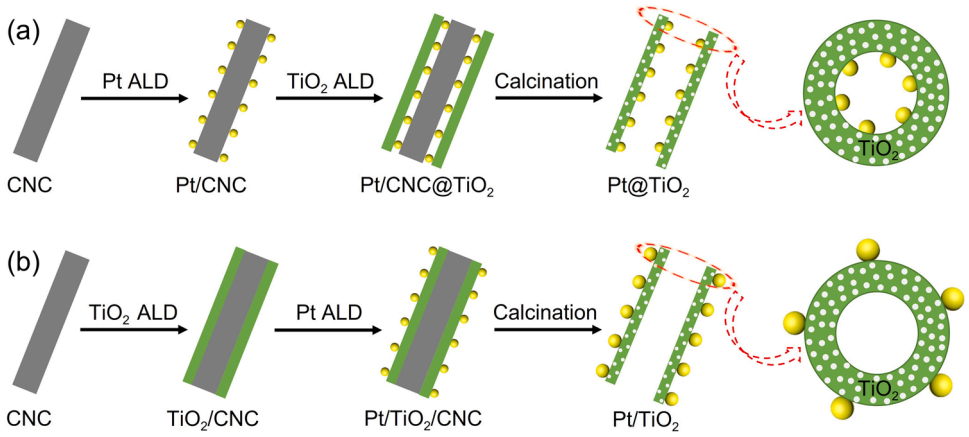

Scheme 1. The synthetic process of the (a) confined Pt@TiO_2 and (b) supported Pt/TiO_2 catalysts.

specific structure is of high necessity.

ALD is a promising alternative technique for the synthesis of conformal thin films and high-dispersion nanoparticles at atomic level [38–49]. It has been extensively applied in catalysis field for synthesizing catalytic materials with specific structures [38–49]. Herein we synthesized the porous TiO_2 nanotube confined Pt@TiO_2 catalysts by carbon nanocoil (CNC) template-assisted ALD approach and investigated the confinement effect of the nanotubes toward Pt nanoparticles. The catalysts were tested in hydrolytic dehydrogenation reaction of ammonia borane (NH_3BH_3, AB). The present approach has excellent controllability and reliability in achieving the confinement of metal nanoparticles and thickness regulation of nanotube walls. Compared with the supported Pt/TiO_2 catalysts, the confined Pt@TiO_2 catalysts exhibit much better catalytic activity and stability in the hydrolytic reaction due to the unique confinement effect.

2. Experimental section

2.1. Catalyst preparation

CNCs were prepared by a slightly modified chemical vapor deposition approach, and the detailed preparation and pretreatment processes can be found in our previous work [49,50]. The ALD processes were performed in a homemade hot-wall reactor. Pt and NiO were deposited at 280 °C (setting temperature) with $MeCpPtMe_3$ and $NiCp_2$ as the corresponding precursors reacting with O_3, which were maintained at

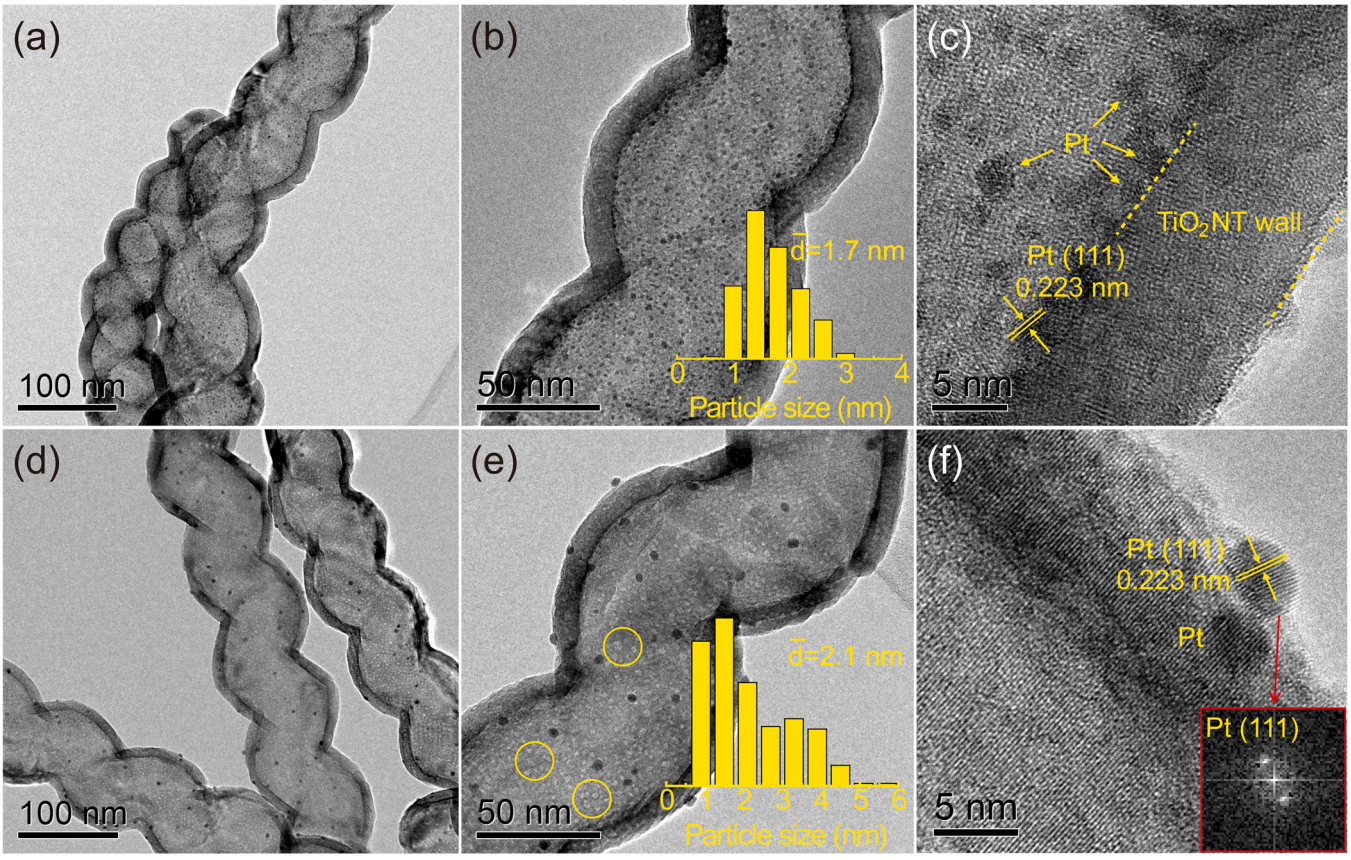

Fig. 1. Low and high magnification TEM and HRTEM images of the (a-c) Pt@TiO_2 and (d-f) Pt/TiO_2 catalysts (Insets of panel b and e: the corresponding histograms of Pt particle size distribution of the two catalysts, respectively). The number of Pt and TiO_2 ALD cycles is 20 and 300 respectively unless otherwise denoted.

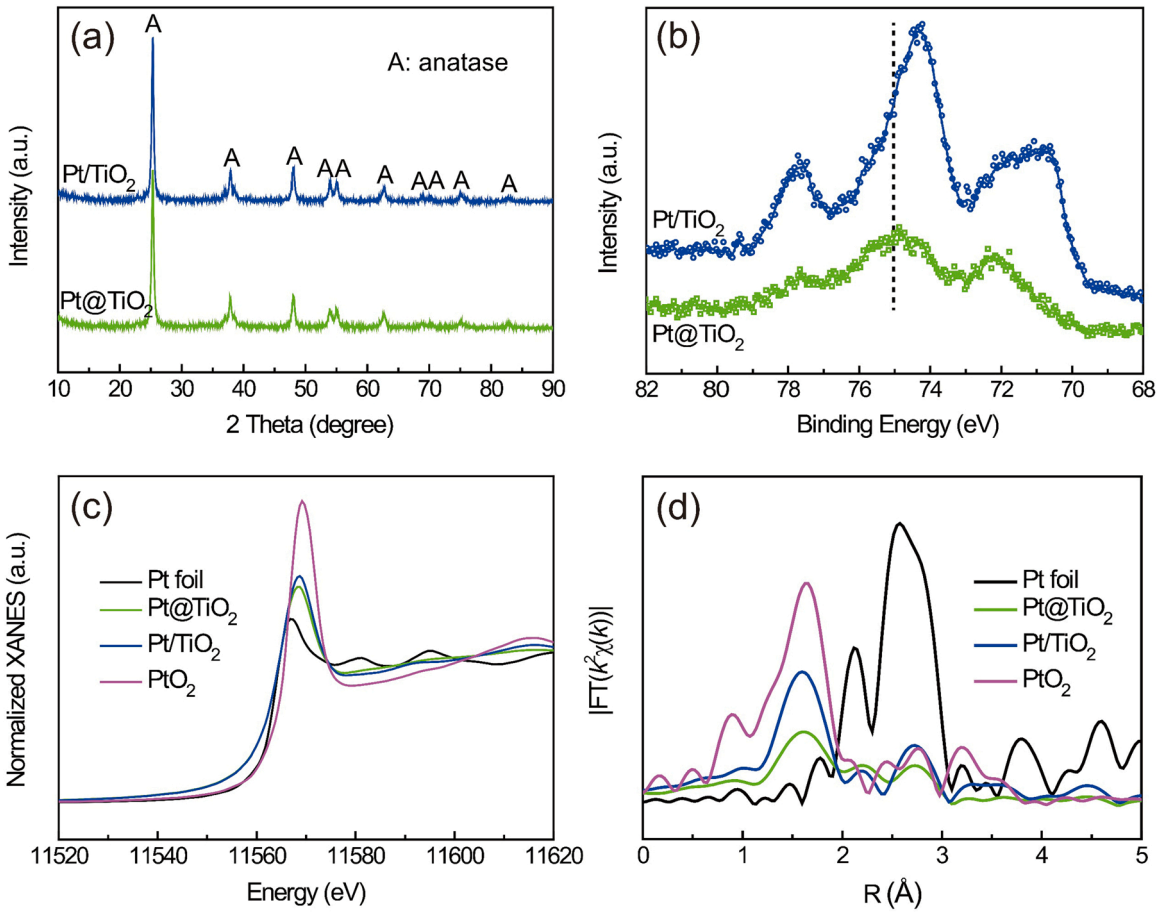

Fig. 2. (a) XRD patterns and (b) XPS Pt 4f spectra of the two catalysts. Normalized Pt L_3-edge (c) XANES and (d) EXAFS spectra of Pt@TiO_2, Pt/TiO_2, Pt foil and PtO_2.

60 °C and 68 °C, respectively. The TiO_2 and Al_2O_3 films were deposited at 125 °C with titanium tetraisopropoxide (TTIP) and trimethylaluminum (TMA) as the corresponding precursors reacting with deionized H_2O, respectively. TTIP was maintained at 80 °C, and both TMA and deionized H_2O were maintained at room temperature.

2.2. Catalyst characterizations

Transmission electron microscopy (TEM) and high-resolution TEM (HRTEM) images were taken with a JEOL-2100 F field-emission transmission electron microscope operated at 200 kV, and the high-angle annular dark-field scanning TEM (HAADF-STEM) and energy-dispersive X-ray spectroscopy mapping images were collected on a FEI-Themis Z instrument operated at 300 kV. The scanning electron microscopy (SEM) images were obtained by a scanning electron microscope (ZEISS Sigma 500, USA). The X-ray diffraction (XRD) patterns were collected using a Philips X'Pert Pro Super X-ray diffractometer with Cu Kα radiation (λ = 1.540 Å). The X-ray photoelectron spectroscopy (XPS) was performed on an ESCALab-250Xi X-ray photoelectron spectrometer (Thermo Fisher Scientific) with an Al Kα source. X-ray absorption fine structure spectra of the Pt L_3-edge were measured on the BL14W1 beamline of the Shanghai Synchrotron Radiation Facility. All the samples measured in the transmission mode. N_2 adsorption-desorption experiments were conducted on a BSD-PS(M) analyzer at 77 K (Beishide Instrument Technology (Beijing) Co., Ltd.). The metal content of the catalysts was determined by inductively coupled plasma optical emission spectroscopy.

2.3. Catalytic activity evaluation

Hydrolytic dehydrogenation of AB: A certain amounts of catalysts and deionized water (typically 10 mL) were added into a round-bottom flask, then AB (typically 1.5 mmol) was added into the flask under stirring conditions. The volume of evolved hydrogen was measured in a water-filled graduated U-type buret system. For the stability experiments, another equivalent of AB was added into the reactor when the remaining H_2 in the reaction system was exhausted after the completion of reaction.

Catalytic hydrogenation of quinoline: The hydrogenation reaction of quinoline was conducted in a stainless steel autoclave reactor. Typically, 100 μL of quinoline, 20 mg of catalysts and 30 mL of ethanol solvent were loaded into the reactor, which was then purged with pure H_2 three times and charged with 2 MPa of H_2. The reaction was performed at 60 °C. After the reaction, the reactants and products were analyzed and quantified by gas chromatographic mass spectrometry (Agilent, 7890 A).

3. Results and discussion

3.1. Comparison of the confined Pt@TiO_2 and supported Pt/TiO_2 catalysts

The porous hollow TiO_2 nanotube confined Pt@TiO_2 and supported Pt/TiO_2 catalysts were synthesized by the template-assisted ALD approach (Scheme 1). For the synthesis of Pt@TiO_2, the ultrafine Pt nanoparticles were firstly deposited on CNCs by Pt ALD, and then an amorphous TiO_2 film was deposited by TiO_2 ALD acquiring the Pt/CNC@TiO_2 composites. The CNC templates were then removed by the

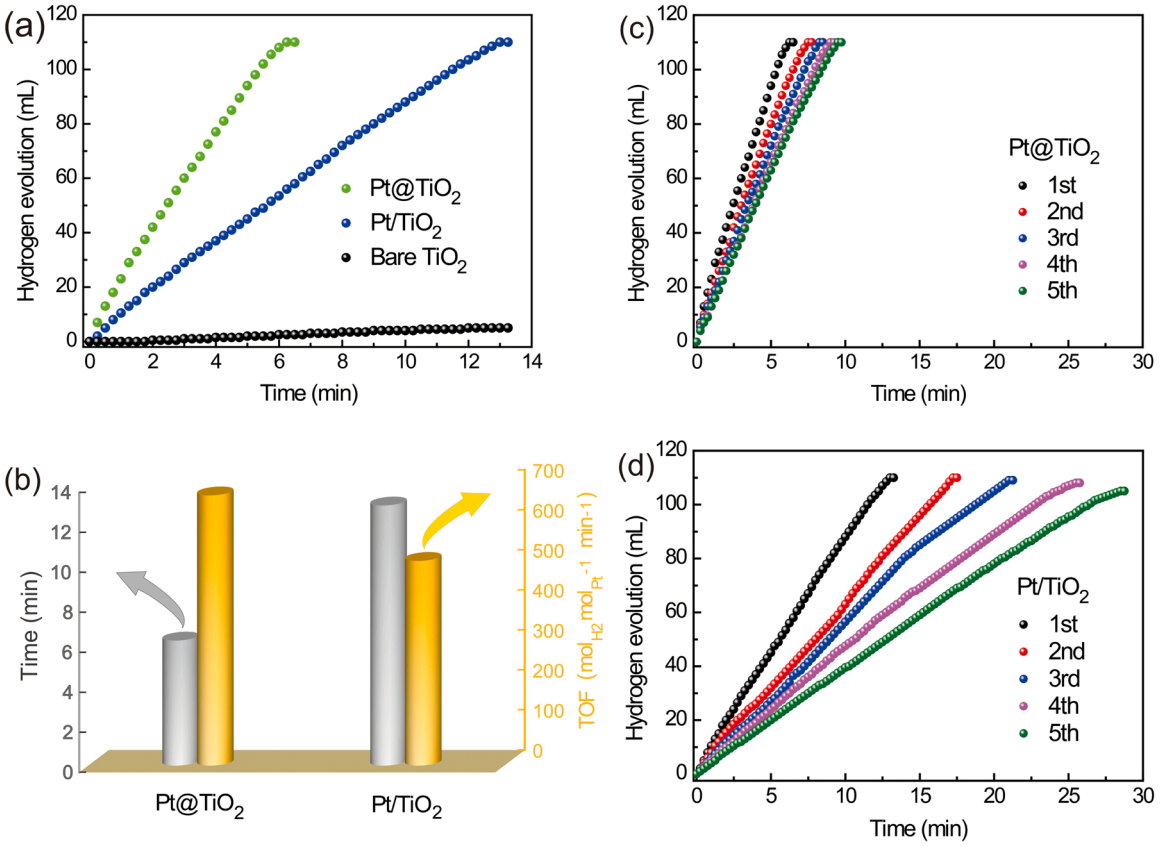

Fig. 3. (a) Volume of hydrogen evolved as a function of time for AB dehydrogenation reaction (0.15 mol/L AB, 25 °C) over the $Pt@TiO_2$, Pt/TiO_2 and bare TiO_2 catalysts. (b) The reaction time and the corresponding TOF values of the $Pt@TiO_2$ and Pt/TiO_2 catalysts. Cycling stability tests of (c) $Pt@TiO_2$ and (d) Pt/TiO_2 catalysts.

calcination process, and the porous nanotube confined $Pt@TiO_2$ catalysts were achieved (Scheme 1a). Similarly, the supported Pt/TiO_2 catalysts were also synthesized by exchanging the deposition sequences of Pt and TiO_2, as schematically illustrated in Scheme 1b. Resultantly, the Pt nanoparticles are loaded on the inner and outer surfaces of TiO_2 nanotubes, achieving the confined $Pt@TiO_2$ and supported Pt/TiO_2 catalysts, respectively.

To determine the microstructure and particle size of the $Pt@TiO_2$ and Pt/TiO_2 catalysts, TEM and HRTEM were performed (Fig. 1). From the TEM and HRTEM images of the confined $Pt@TiO_2$ catalysts (Fig. 1a-c and S1a), the highly dispersed Pt nanoparticles with the average particle size of approximately 1.7 nm (inset of Fig. 1b) are confined on the inner surfaces of the TiO_2 nanotubes. Note that no obvious nanoparticle agglomeration is observed though the catalysts are calcined under the high temperature (500 °C-1.5 h), which can be ascribed to the remarkable confinement effect of TiO_2 nanotubes toward Pt nanoparticles inhibiting the migration and growth of Pt nanoparticles. Fig. 1c shows the typical HRTEM image of the $Pt@TiO_2$ catalysts, and the measured lattice fringe distance of the Pt nanoparticle is approximately 0.223 nm (also see Fig. 1f), which matches well with the Pt(111) plane [40]. The porous TiO_2 nanotubes with a wall thickness of about 12 nm can be observed clearly, and the crystallized layer corresponds to the anatase TiO_2 (also see XRD results below) [49]. The uniformly distributed white dots (as circled in Fig. 1e) are the formed nanopores on the TiO_2 nanotube walls after the calcination process. While for the supported Pt/TiO_2 catalysts, the Pt nanoparticles are anchored on the outer surfaces of TiO_2 nanotubes (Figs. 1d-f and S1b), and the average particle size is about 2.1 nm (inset of Fig. 1e), and this value is higher than that of the confined $Pt@TiO_2$ counterparts. Note that the particle size distribution of the Pt/TiO_2 catalysts is much wider than that of the $Pt@TiO_2$ counterparts and many nanoparticles with larger size (> 3 nm) can be clearly observed on the Pt/TiO_2 catalysts. The formation of ultrafine Pt nanoparticles with smaller size and narrow distribution on the $Pt@TiO_2$ catalysts should be ascribed to the confinement effect TiO_2 nanotubes inhibiting the agglomeration and growth of the nanoparticles.

Fig. 2a is the XRD patterns of $Pt@TiO_2$ and Pt/TiO_2 catalysts. The characteristic diffraction peak at $2\theta = 25.3°$ accompanied with several weak peaks can be observed, which are readily indexed to the anatase TiO_2 (JCPDS No.21–1272). No peak related to Pt or PtO_x is observed from the XRD patterns due to the high dispersion and low contents of the Pt nanoparticles ($Pt@TiO_2$: 1.04 wt% versus Pt/TiO_2: 0.66 wt%). However, the Pt 4f peaks can be well dectected from the XPS spectra of the two catalysts (Figs. 2b and S2). The Pt 4f binding energy of Pt/TiO_2 shifts to a lower position compared with that of $Pt@TiO_2$, which should be due to the metal nanoparticle size effects and electronic metal-support interactions [25,51,52]. Additionally, both the catalysts present an obvious peak at around 77.8 eV, indicating the existence of Pt species with higher valence states. This can be further verified by X-ray absorption fine structure spectroscopy characterization. From the X-ray absorption near-edge structure (XANES, Fig. 2c) and extended X-ray absorption fine structure (EXAFS, Fig. 2d) spectra, the white-line intensities of the two catalysts locate between that of Pt foil and PtO_2, and Pt-O (1.6 Å) and Pt-Pt (2.7 Å) bonds are both detected, indicating the existence of metallic platinum and platinum oxide species in the as-prepared Pt catalysts. The $Pt@TiO_2$ catalysts present lower white line peak intensity, suggesting the slightly lower valence state, which should be ascribed to the protection effect of TiO_2 shell toward Pt nanoparticles reducing the exposure of Pt nanoparticles with air.

The hydrolytic dehydrogenation reaction of AB is a typical structure-sensitive reaction [53–63], which is chose to evaluate the catalytic performances of the catalysts. It can be observed that the H_2 can be readily released through the hydrolytic route and the confined $Pt@TiO_2$

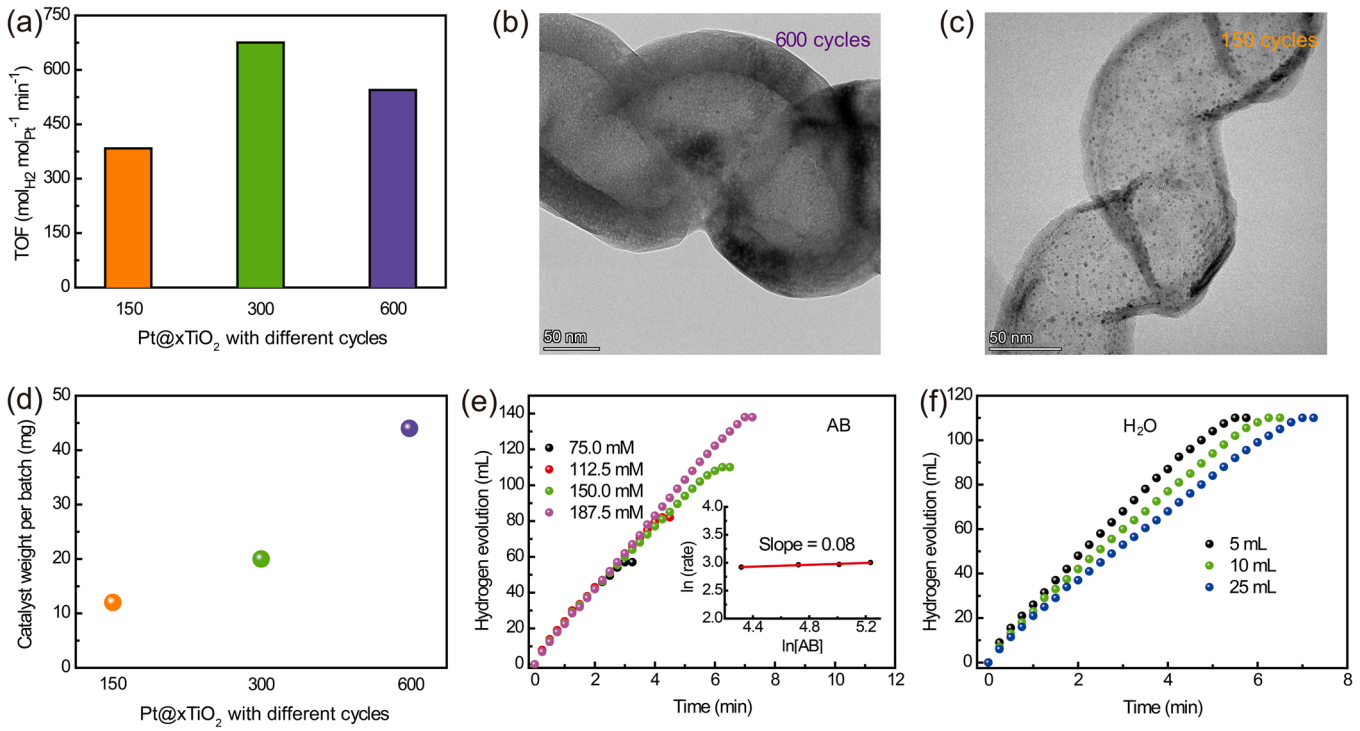

Fig. 4. (a) TOF values of the Pt@TiO_2 catalysts with different TiO_2 ALD cycles (wall thickness, x is the number of TiO_2 ALD cycles). The TEM images of Pt@TiO_2 catalysts with (b) 600-cycle and (c) 150-cycle TiO_2. (d) Weight of the catalysts with different TiO_2 ALD cycles per batch (quartz wafer). Amounts of (e) AB and (f) H_2O on the influence of the hydrolytic dehydrogenation activity over the optimized Pt@TiO_2 catalysts (Inset of Fig. 4e: the logarithmic plot of reaction rate versus AB concentration).

catalysts present remarkably higher H_2 evolution activity than the supported Pt/TiO_2 counterparts (Fig. 3a and b). The calculated turnover frequency (TOF) value is approximately 675.3 mol_{H2} mol_{Pt}^{-1} min^{-1} for the confined Pt@TiO_2 catalysts, which is about 1.3 times as high as that of the supported Pt/TiO_2 counterparts (511.6 mol_{H2} mol_{Pt}^{-1} min^{-1}, Fig. 3b). Note that the bare TiO_2 presents very poor activity, and only 5 mL of H_2 is evolved in 13 min. Similarly, the confined Pt@TiO_2 catalysts still exhibit higher activity than the supported Pt/TiO_2 counterparts with a higher content (25-cycle Pt, Fig. S3), which again confirms the superiority of the confined catalysts. Additionally, the stability tests of the two catalysts were also conducted (Fig. 3c and d). Obviously, the confined Pt@TiO_2 catalysts exhibit much better stability than the supported Pt/TiO_2 counterparts due to the confinement effect, although the confined catalysts still present somewhat decreased activity during

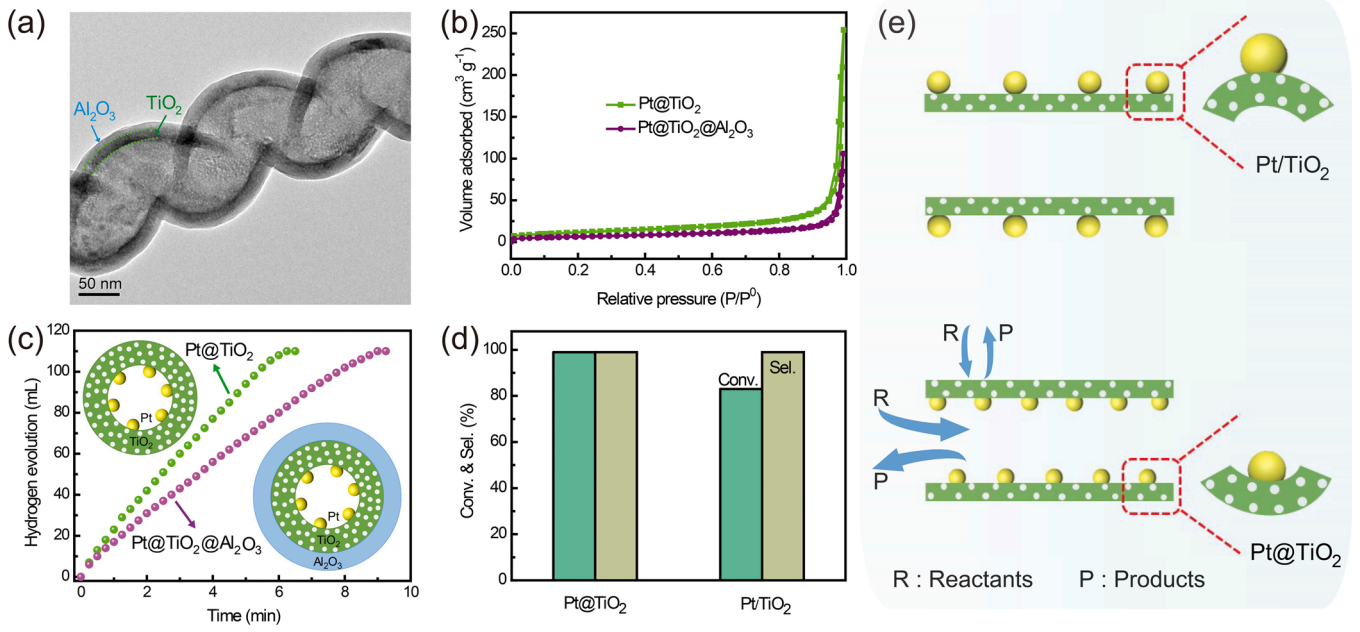

Fig. 5. (a) TEM image of the Pt@TiO_2@Al_2O_3 catalysts. (b) N_2 adsorption-desorption isotherms of the Pt@TiO_2 and Pt@TiO_2@Al_2O_3 catalysts. (c) The comparison of the dehydrogenation activity over the Pt@TiO_2 and Pt@TiO_2@Al_2O_3 catalysts. (d) Selective hydrogenation of quinoline results over the Pt@TiO_2 and Pt/TiO_2 catalysts. (e) Schematic illustration of the interfacial structures and reaction channels for the two catalysts (The white dots represent nanopores of nanotube walls).

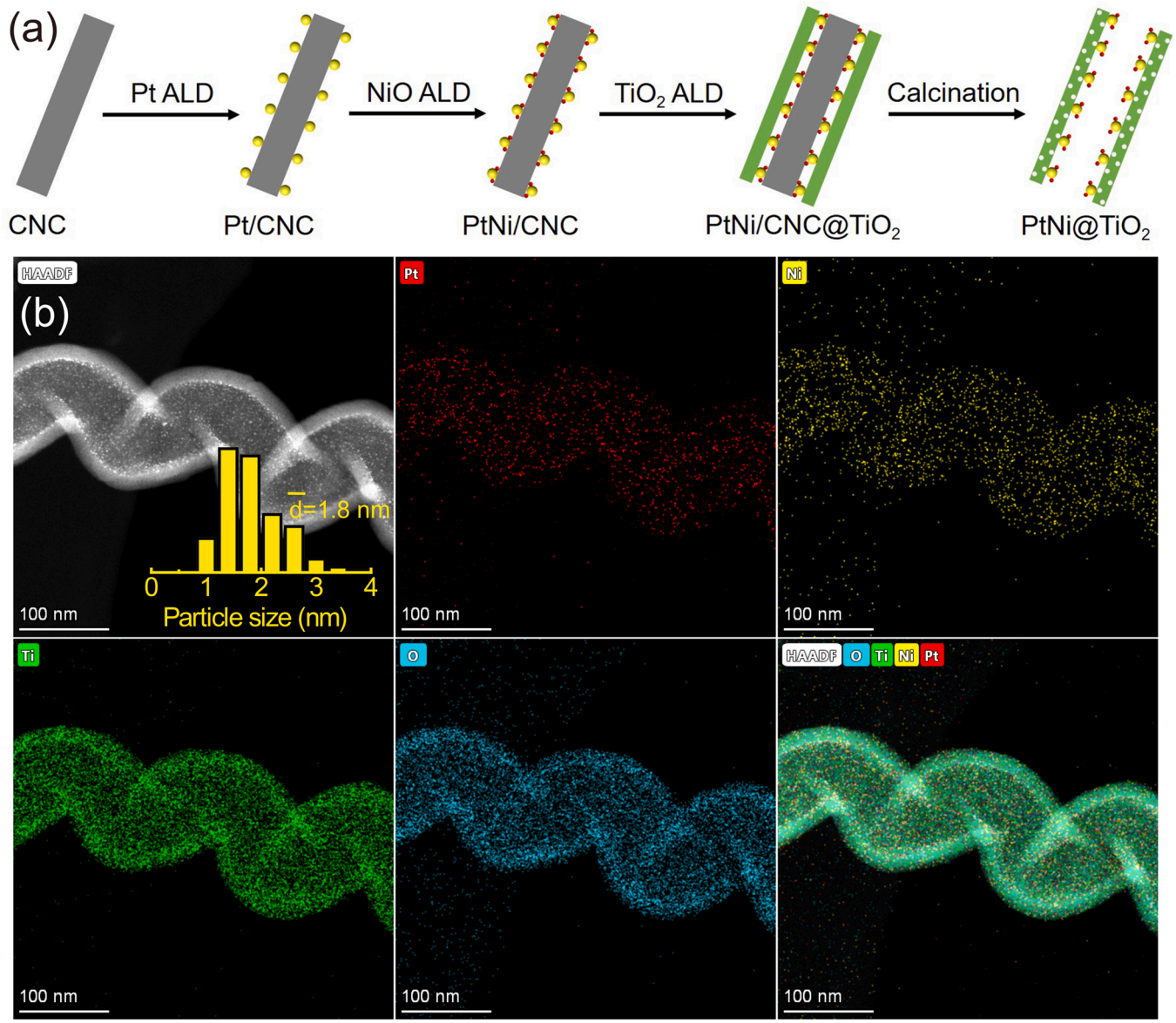

Fig. 6. (a) The synthetic process of the confined PtNi@TiO_2 bicomponent catalysts. (b) HAADF-STEM (Inset: the histogram of the particle size distribution) and the corresponding Pt, Ni, Ti, O and overlapped elemental mapping images of the PtNi@TiO_2 catalysts.

the recycle tests. This should be ascribed to the poisonous effect of B-containing by-products on the Pt nanoparticles and the deformation-agglomeration of Pt nanoparticles (Fig. S1c and d) [39,62].

The thickness of TiO_2 nanotube wall generally has a significant influence on the catalytic performances. Therefore, the confined Pt@TiO_2 catalysts with different thickness of nanotube walls were synthesized, which could be achieved by simply varying the number of TiO_2 ALD cycles. As shown in Figs. 4a and S4, the Pt@TiO_2 catalysts with proper thickness (300-cycle TiO_2) exhibit the optimized catalytic dehydrogenation activity, and the further increase of the wall thickness of TiO_2 nanotubes (ca. 37.5 nm, 600-cycle TiO_2, Fig. 4b) results in the decreased activity due to the diffusion depression of the reacting molecules through the nanopores of nanotube walls. This result also indicates that the nanopores are probably the via holes, and the reacting molecules are diffused mainly through the open ends instead of the nanopores. While an obvious decline of the dehydrogenation activity can be observed when the wall thickness is too thin (ca. 6.5 nm, 150-cycle TiO_2, Fig. 4c). This should be ascribed to the potential structural collapse of the catalysts during the calcination as well as the intense stirring reaction processes (Fig. S5), which would result in the partial cover of Pt nanoparticles and the corresponding decline of the dehydrogenation activity. Therefore, the proper wall thickness is of great necessity to achieve the confined catalysts with well-preserved structure and excellent catalytic activity. Factually, the successful tuning toward wall thickness can also be verified by the mass changes of catalysts per batch (Fig. 4d). In addition, the amounts of the AB and H_2O on the influence of the dehydrogenation activity over the optimized Pt@TiO_2 catalysts were also performed. The dehydrogenation rates are almost unchanged with the variation of AB concentration (Fig. 4e) and the line slope of ln(rate) versus ln[AB] is about 0.08, indicating that the hydrolytic reaction is a pseudo 0 order reaction for the AB. Fig. 4f presents the influence of H_2O amount on the reaction rates, and the increased H_2O amounts are not advantageous for the enhancement of dehydrogenation activity.

To further confirm the roles of the open ends and nanopores of TiO_2 nanotube wall played during the reaction, we designed and synthesized the dense Al_2O_3 layer coated Pt@TiO_2 @Al_2O_3 reference catalysts with negligible nanopores (Scheme S1), that is, the Pt@TiO_2 catalysts were further coated with a dense Al_2O_3 layer with a thickness of approximately 7 nm (Fig. 5a). The N_2 adsorption-desorption characterization (Fig. 5b) also confirms the successful coating of the dense Al_2O_3 layer on

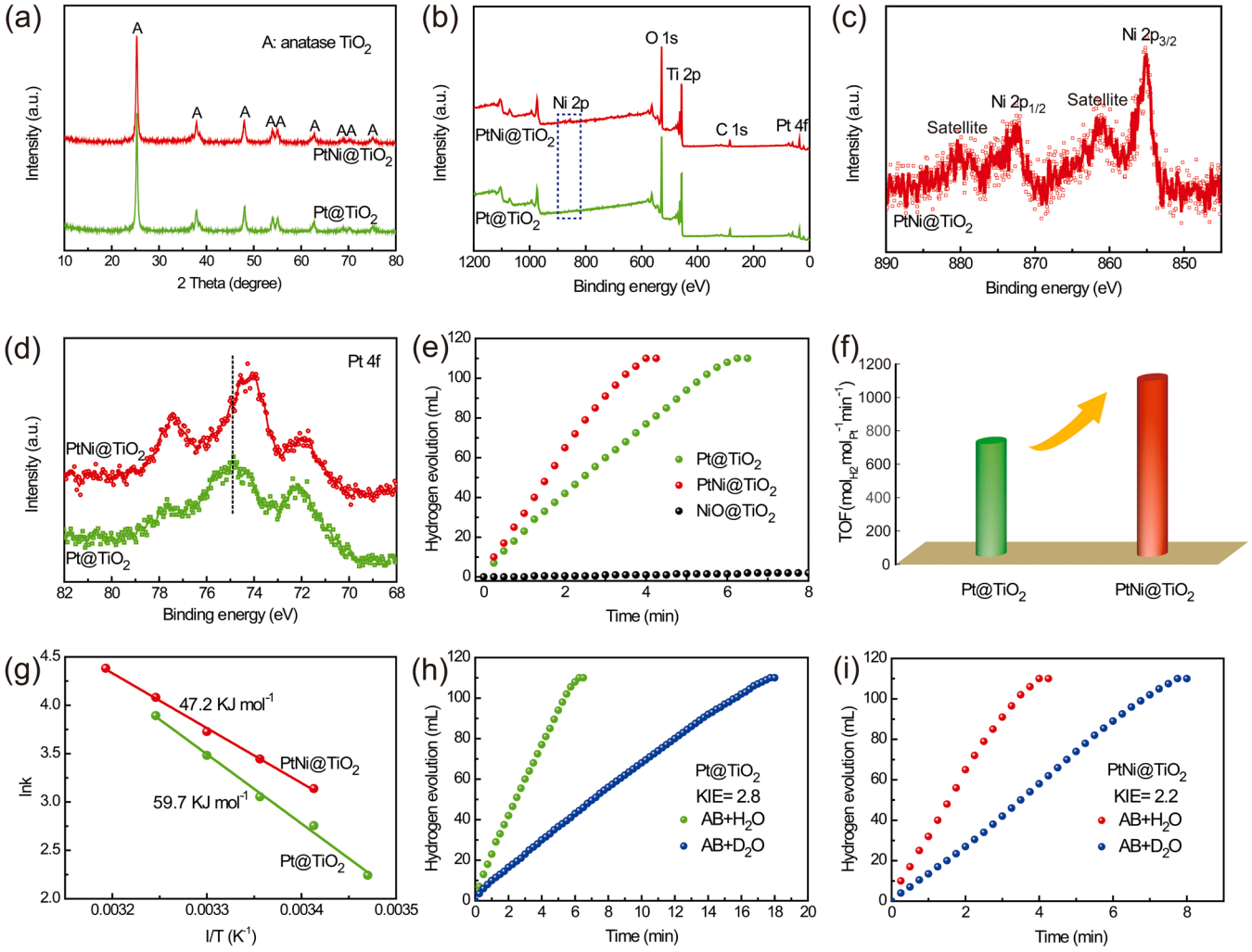

Fig. 7. (a) XRD patterns and (b) XPS survey spectra of the Pt@TiO_2 and PtNi@TiO_2 catalysts. (c) XPS Ni 2p spectrum of the PtNi@TiO_2 catalysts. (d) XPS Pt 4f spectra of the Pt@TiO_2 and PtNi@TiO_2 catalysts. (e) Volume of hydrogen evolved as a function of time for the hydrolytic dehydrogenation reaction (0.15 mol/L AB, 25 °C) over Pt@TiO_2, PtNi@TiO_2 and reference NiO@TiO_2 catalysts. (f) The comparison of TOF values of the two catalysts. (g) The Arrhenius plots and the corresponding E_a of the two catalysts. The measurements of KIE values over the (h) Pt@TiO_2 and (i) PtNi@TiO_2 catalysts.

the Pt@TiO_2 catalysts. After the coating of the dense Al_2O_3 layer, the specific surface area and total pore volume of the Pt@TiO_2 catalysts decrease from 41.7 m^2 g^{-1} and 0.34 cm^3 g^{-1} to 22.6 m^2 g^{-1} and 0.15 cm^3 g^{-1}, respectively. As expected, the dehydrogenation activity deceases by approximately 30% after blocking the nanopores of TiO_2 nanotube walls by the dense Al_2O_3 layer (Fig. 5c). Note that the AB molecules, in this case, can still access the inner Pt nanoparticles through the large open ends. That is to say, the open ends should be the main diffusion channels for the reactant/product molecules. In addition, the selective hydrogenation of quinoline tests were also conducted to further verify the confinement effect of the porous nanotubes (Figs. 5d and S6), and the result indicates that the confined catalysts still present higher hydrogenation activity.

Combined with the above results, the potential enhancement mechanism for the confined Pt@TiO_2 catalysts is discussed. It is true that both the open ends and nanopores of the TiO_2 nanotubes can provide the diffusion channels for the reacting molecules. While it should be noted that the size of open ends of nanotubes, corresponding to the diameter of CNCs (Fig. S7), is much larger than that of the nanopores (ca. 2 nm) on the nanotube walls, which should be the main diffusion channels for the reacting molecules (Fig. 5e). The combined effects of the two channels make the diffusion and access of reactant molecules to the inner Pt nanoparticles and the desorption of H_2 product molecules with negligible diffusion resistance, as the case for the Pt/TiO_2 catalysts. Furthermore, the Pt@TiO_2 catalysts possess the smaller particle size compared with the Pt/TiO_2 counterparts due to the remarkable confinement effect of porous nanotubes toward Pt nanoparticles, which makes the Pt@TiO_2 catalysts possess more active sites and thus present higher catalytic activity. In addition, the confined Pt@TiO_2 catalysts possess larger number of Pt-TiO_2 interface sites (semi-embedded interfaces, Fig. 5e) than Pt/TiO_2 counterparts, and the interfacial regions are generally considered to be catalytically active [64–66]. The synergistic effects of the factors lead to the boosted catalytic activity of the Pt@TiO_2 catalysts. Besides, the larger interfacial regions between Pt and TiO_2, to a certain extent, can also strengthen the metal-support interaction and correspondingly enhance the stability of the confined Pt@TiO_2 catalysts [64].

3.2. *The synthesis and evaluation of bicomponent catalysts*

The present approach is facile and general, which can be extended and applied to prepare the bicomponent catalysts. To this end, we also prepared the confined bicomponent PtNi@TiO_2 catalysts by adding the NiO ALD process after the Pt ALD process (Fig. 6a). From the TEM, HAADF-STEM and the corresponding elemental mapping images (Figs. 6b and S8), the ultrafine bicomponent nanoparticles are

homogeneously decorated on the inner surfaces of TiO_2 nanotubes. The obtained bicomponent PtNi@TiO_2 catalysts have similar particle size distribution compared with the monometallic Pt@TiO_2 catalysts, and the average particle size is approximately 1.8 nm for the PtNi@TiO_2 catalysts (inset of Fig. 6b), which is also similar to that of the Pt@TiO_2 catalysts (1.7 nm). The characterizations by XRD and SEM-EDS mapping images further indicate the homogeneous distribution of the PtNi bicomponent nanoparticles (Fig. 7a and S9). To elucidate the influence of NiO decoration on the electronic state of Pt, XPS characterization was conducted. The results (Fig. 7b-d) indicate that there exists the electron transfer from NiO to Pt leading to the electron-rich state of Pt, which would potentially influence the catalytic performances of the catalysts [39]. To this end, the PtNi@TiO_2 catalysts were also evaluated for catalytic dehydrogenation of AB (Fig. 7e). To our delighted, the needed reaction time decreases to 4 min when using PtNi@TiO_2 as catalysts, and correspondingly the TOF value amounts to 1055.2 mol_{H2} mol_{Pt}^{-1} min^{-1} (Fig. 7f), which is approximately 1.5 times as high as that of Pt@TiO_2 catalysts. Note that NiO@TiO_2 (0.62 wt%, 20-cycle, Fig. S10) catalysts show negligible activity and only ca. 2 mL of H_2 is released in 8 min. To gain a deep insight into the Pt-Ni synergy in the reaction, kinetic and isotopic tests of the two catalysts were conducted. The calculated apparent activation energy (E_a) using the Arrhenius law is approximately 47.2 KJ mol^{-1} for PtNi@TiO_2 catalysts (Figs. 7g and S11), and this value is much lower than that of Pt@TiO_2 counterparts (59.7 KJ mol^{-1}), indicating that the nickel species addition lowers the E_a and correspondingly enhances the dehydrogenation activity. Additionally, the isotopic results show that the PtNi@TiO_2 catalysts exhibit lower kinetic isotope effect value (KIE=2.2, Fig. 7i) compared with the Pt@TiO_2 catalysts (2.8, Fig. 7h), indicating that the synergistic effect of Pt-Ni can facilitate the O-H bond cleavage of H_2O molecules being the rate determining step [39,62,63]. In fact, the present strategy is not limited to the synthesis of the above-mentioned mono-/bicomponent catalysts, which can realize the facile and controllable assembly of different metals/metal oxides (Pd, Ru, CuO_x etc.) and supports (Al_2O_3, SiO_2 etc.) for a given catalytic reaction.

4. Conclusions

In summary, the porous TiO_2 nanotube confined Pt@TiO_2 catalysts with complete confinement present remarkably higher catalytic activity and stability. The ultrafine Pt nanoparticles with smaller size, more Pt-TiO_2 interfacial sites and the porous structures of the nanotubes with proper thickness and large open ends excluding the diffusion influence during the reaction process synergistically contribute to the excellent catalytic performances of the confined catalysts. The TOF value was further enhanced to 1055.2 mol_{H2} mol_{Pt}^{-1} min^{-1} with the confined bicomponent PtNi@TiO_2 as catalysts. The present general approach can be potentially applied to the synthesis of other confined mono-/bicomponent catalysts with specific structure and high performance for various heterogeneous reactions.

CRediT authorship contribution statement

Jiankang Zhang: Conceptualization, Methodology, Investigation, Visualization, Supervision, Writing – review & editing and Funding acquisition. **Wenlong Yu**: Formal analysis, Writing – review & editing. **Dan Feng**: Formal analysis and Validation. Hao Xu: Formal analysis. **Yong Qin**: Supervision, Validation, Writing – review & editing.

Declaration of Competing Interest

The authors declare that they have no known competing financial interests or personal relationships that could have appeared to influence the work reported in this paper.

Acknowledgements

We appreciate the financial support from the National Natural Science Foundation of China (22102131), Natural Science Foundation of Shandong Province (ZR2019BB039), Natural Science Basic Research Plan in Shaanxi Province of China (2021JQ-090) and the Fundamental Research Funds for the Central Universities (G2021KY05103). We would like to thank the Analytical & Testing Center of Northwestern Polytechnical University for HAADF-STEM and Shanghai Synchrotron Radiation Facility for XAFS measurements.

Appendix A. Supporting information

Supplementary data associated with this article can be found in the online version at doi:10.1016/j.apcatb.2022.121405.

References

[1] J. Knossalla, P. Paciok, D. Göhl, D. Jalalpoor, E. Pizzutilo, A.M. Mingers, M. Heggen, R.E. Dunin-Borkowski, K.J. Mayrhofer, F. Schüth, Shape-controlled nanoparticles in pore-confined space, J. Am. Chem. Soc. 140 (2018) 15684–15689.
[2] X. Zhang, M. Zhang, Y. Deng, M. Xu, L. Artiglia, W. Wen, R. Gao, B. Chen, S. Yao, X. Zhang, M. Peng, J. Yan, A. Li, Z. Jiang, X. Gao, S. Cao, C. Yang, A.J. Kropf, J. Shi, J. Xie, M. Bi, J.A. van Bokhoven, Y.-W. Li, X. Wen, M. Flytzani-Stephanopoulos, C. Shi, W. Zhou, D. Ma, A stable low-temperature H_2-production catalyst by crowding Pt on α-MoC, Nature 589 (2021) 396–401.
[3] N. Zhang, Y.-J. Xu, Aggregation- and leaching-resistant, reusable, and multifunctional Pd@CeO_2 as a robust nanocatalyst achieved by a hollow core-shell strategy, Chem. Mater. 25 (2013) 1979–1988.
[4] Z. Guo, C. Xiao, R.V. Maligal-Ganesh, L. Zhou, T.W. Goh, X. Li, D. Tesfagaber, A. Thiel, W. Huang, Pt nanoclusters confined within metal-organic framework cavities for chemoselective cinnamaldehyde hydrogenation, ACS Catal. 4 (2014) 1340–1348.
[5] J. Zhang, L. Wang, B. Zhang, H. Zhao, U. Kolb, Y. Zhu, L. Liu, Y. Han, G. Wang, C. Wang, D. Su, B.C. Gates, F.-S. Xiao, Sinter-resistant metal nanoparticle catalysts achieved by immobilization within zeolite crystals via seed-directed growth, Nat. Catal. 1 (2018) 540–546.
[6] H. Zhang, M. Huang, J. Wen, Y. Li, A. Li, L. Zhang, A.M. Ali, Y. Li, Sub-3 nm Rh nanoclusters confined within a metal-organic framework for enhanced hydrogen generation, Chem. Commun. 55 (2019) 4699–4702.
[7] Q. Yang, Q. Xu, S.H. Yu, H.L. Jiang, Pd nanocubes@ZIF-8: integration of plasmon-driven photothermal conversion with a metal-organic framework for efficient and selective catalysis, Angew. Chem. Int. Ed. 128 (2016) 3749–3753.
[8] T.A. Shifa, A. Vomiero, Confined catalysis: progress and prospects in energy conversion, Adv. Energy Mater. 9 (2019), 1902307.
[9] K. Yoon, Y. Yang, P. Lu, D. Wan, H.C. Peng, K. Stamm Masias, P.T. Fanson, C. T. Campbell, Y. Xia, A highly reactive and sinter-resistant catalytic system based on platinum nanoparticles embedded in the inner surfaces of CeO_2 hollow fibers, Angew. Chem. Int. Ed. 51 (2012) 9543–9546.
[10] Q. Fu, X. Bao, Confined microenvironment for catalysis control, Nat. Catal. 2 (2019) 834–836.
[11] H. Tabassum, A. Mahmood, B. Zhu, Z. Liang, R. Zhong, S. Guo, R. Zou, Recent advances in confining metal-based nanoparticles into carbon nanotubes for electrochemical energy conversion and storage devices, Energy Environ. Sci. 12 (2019) 2924–2956.
[12] S. Wang, Z. Zhao, X. Chang, J. Zhao, H. Tian, C. Yang, M. Li, Q. Fu, R. Mu, J. Gong, Activation and spillover of hydrogen on sub-1nm palladium nanoclusters confined within sodalite zeolite for the semi-hydrogenation of alkynes, Angew. Chem. Int. Ed. 58 (2019) 7668–7672.
[13] J. Hu, Y. Ren, L. Zhang, Dual-confined SeS_2 cathode based on polyaniline-assisted double-layered micro/mesoporous carbon spheres for advanced Li-SeS_2 battery, J. Power Sources 455 (2020), 227955.
[14] H. Peng, X. Zhang, X. Han, X. You, S. Lin, H. Chen, W. Liu, X. Wang, N. Zhang, Z. Wang, P. Wu, H. Zhu, S. Dai, Catalysts in coronas: a surface spatial confinement strategy for high-performance catalysts in methane dry reforming, ACS Catal. 9 (2019) 9072–9080.
[15] L. Liu, U. Diaz, R. Arenal, G. Agostini, P. Concepcion, A. Corma, Generation of subnanometric platinum with high stability during transformation of a 2D zeolite into 3D, Nat. Mater. 16 (2017) 132–138.
[16] H.J. Cho, D. Kim, J. Li, D. Su, B. Xu, Zeolite-encapsulated Pt nanoparticles for tandem catalysis, J. Am. Chem. Soc. 140 (2018) 13514–13520.
[17] C. Wang, L. Wang, J. Zhang, H. Wang, J.P. Lewis, F.-S. Xiao, Product selectivity controlled by zeolite crystals in biomass hydrogenation over a palladium catalyst, J. Am. Chem. Soc. 138 (2016) 7880–7883.
[18] Q. Sun, N. Wang, R. Bai, Y. Hui, T. Zhang, D.A. Do, P. Zhang, L. Song, S. Miao, J. Yu, Synergetic effect of ultrasmall metal clusters and zeolites promoting hydrogen generation, Adv. Sci. 6 (2019), 1802350.
[19] N. Wang, Q. Sun, J. Yu, Ultrasmall metal nanoparticles confined within crystalline nanoporous materials: a fascinating class of nanocatalysts, Adv. Mater. 31 (2019), 1803966.

[20] S.-M. Wu, X.-Y. Yang, C. Janiak, Confinement effects in zeolite-confined noble metals, Angew. Chem. Int. Ed. 131 (2019) 12468–12482.
[21] W. Zhang, G. Lu, C. Cui, Y. Liu, S. Li, W. Yan, C. Xing, Y.R. Chi, Y. Yang, F. Huo, A family of metal-organic frameworks exhibiting size-selective catalysis with encapsulated noble-metal nanoparticles, Adv. Mater. 26 (2014) 4056–4060.
[22] X. Yang, J.-K. Sun, M. Kitta, H. Pang, Q. Xu, Encapsulating highly catalytically active metal nanoclusters inside porous organic cages, Nat. Catal. 1 (2018) 214.
[23] L. Jiao, Y. Wang, H.L. Jiang, Q. Xu, Metal-organic frameworks as platforms for catalytic applications, Adv. Mater. 30 (2018), 1703663.
[24] H. Tian, J. Liang, J. Liu, Nanoengineering carbon spheres as nanoreactors for sustainable energy applications, Adv. Mater. 31 (2019), 1903886.
[25] Z. Yu, N. Ji, J. Xiong, X. Li, R. Zhang, L. Zhang, X. Lu, Ruthenium-nanoparticle-loaded hollow carbon spheres as nanoreactors for hydrogenation of levulinic acid: explicitly recognizing the void-confinement effect, Angew. Chem. Int. Ed. 133 (2021) 2–10.
[26] C. Gao, F. Lyu, Y. Yin, Encapsulated metal nanoparticles for catalysis, Chem. Rev. 121 (2020) 834–881.
[27] W. Zhu, Z. Chen, Y. Pan, R. Dai, Y. Wu, Z. Zhuang, D. Wang, Q. Peng, C. Chen, Y. Li, Functionalization of hollow nanomaterials for catalytic applications: nanoreactor construction, Adv. Mater. 31 (2019), 1800426.
[28] V. Mouarrawis, R. Plessius, J.I. van der Vlugt, J.N. Reek, Confinement effects in catalysis using well-defined materials and cages, Front. Chem. 6 (2018) 623.
[29] H.O. Otor, J.B. Steiner, C. García-Sancho, A.C. Alba-Rubio, Encapsulation methods for control of catalyst deactivation: a review, ACS Catal. 10 (2020) 7630–7656.
[30] W. Chen, Z. Fan, X. Pan, X. Bao, Effect of confinement in carbon nanotubes on the activity of fischer-tropsch iron catalyst, J. Am. Chem. Soc. 130 (2008) 9414–9419.
[31] X. Pan, X. Bao, The effects of confinement inside carbon nanotubes on catalysis, Acc. Chem. Res. 44 (2011) 553–562.
[32] Z. Chen, Z. Guan, M. Li, Q. Yang, C. Li, Enhancement of the performance of a platinum nanocatalyst confined within carbon nanotubes for asymmetric hydrogenation, Angew. Chem. Int. Ed. 123 (2011) 5015–5019.
[33] S.A. Miners, G.A. Rance, A.N. Khlobystov, Chemical reactions confined within carbon nanotubes, Chem. Soc. Rev. 45 (2016) 4727–4746.
[34] X. Yang, X. Yu, L. Long, T. Wang, L. Ma, L. Wu, Y. Bai, X. Li, S. Liao, Pt nanoparticles entrapped in titanate nanotubes (TNT) for phenol hydrogenation: the confinement effect of TNT, Chem. Commun. 50 (2014) 2794–2796.
[35] H. Wang, L. Wu, A. Jia, X. Li, Z. Shi, M. Duan, Y. Wang, Ni nanoparticles encapsulated in the channel of titanate nanotubes: Efficient noble-metal-free catalysts for selective hydrogen generation from hydrous hydrazine, Chem. Eng. J. 332 (2018) 637–646.
[36] H. Yue, Y. Zhao, S. Zhao, B. Wang, X. Ma, J. Gong, A copper-phyllosilicate core-sheath nanoreactor for carbon-oxygen hydrogenolysis reactions, Nat. Commun. 4 (2013) 2339.
[37] D. Yao, Y. Wang, K. Hassan-Legault, A. Li, Y. Zhao, J. Lv, S. Huang, X. Ma, Balancing effect between adsorption and diffusion on catalytic performance inside hollow nanostructured catalyst, ACS Catal. 9 (2019) 2969–2976.
[38] Z. Gao, G. Wang, T. Lei, Z. Lv, M. Xiong, L. Wang, S. Xing, J. Ma, Z. Jiang, Y. Qin, Enhanced hydrogen generation by reverse spillover effects over bicomponent catalysts, Nat. Commun. 13 (2022) 118.
[39] J. Zhang, X. Zheng, W. Yu, X. Feng, Y. Qin, Unravelling the synergy in platinum-nickel bimetal catalysts designed by atomic layer deposition for efficient hydrolytic dehydrogenation of ammonia borane, Appl. Catal. B Environ. 306 (2022), 121116.
[40] J. Zhang, W. Chen, H. Ge, C. Chen, W. Yan, Z. Gao, J. Gan, B. Zhang, X. Duan, Y. Qin, Synergistic effects in atomic-layer-deposited PtCox/CNTs catalysts enhancing hydrolytic dehydrogenation of ammonia borane, Appl. Catal. B Environ. 235 (2018) 256–263.
[41] J. Lu, J.W. Elam, P.C. Stair, Synthesis and stabilization of supported metal catalysts by atomic layer deposition, Acc. Chem. Res. 46 (2013) 1806–1815.
[42] M.A. Khalily, H. Eren, S. Akbayrak, H.H. Susapto, N. Biyikli, S. Özkar, M.O. Guler, Facile synthesis of three-dimensional Pt-TiO_2 nano-networks: a highly active catalyst for the hydrolytic dehydrogenation of ammonia-borane, Angew. Chem. Int. Ed. 128 (2016) 12445–12449.
[43] X. Meng, X. Wang, D. Geng, C. Ozgit-Akgun, N. Schneider, J.W. Elam, Atomic layer deposition for nanomaterial synthesis and functionalization in energy technology, Mater. Horiz. 4 (2017) 133–154.
[44] X. Liu, Q. Zhu, Y. Lang, K. Cao, S. Chu, B. Shan, R. Chen, Oxide-nanotrap-anchored platinum nanoparticles with high activity and sintering resistance by area-selective atomic layer deposition, Angew. Chem. Int. Ed. 129 (2017) 1670–1674.
[45] J.A. Singh, N. Yang, S.F. Bent, Nanoengineering heterogeneous catalysts by atomic layer deposition, Annu. Rev. Chem. Biomol. Eng. 8 (2017) 41–62.
[46] H. Yan, K. He, I.A. Samek, D. Jing, M.G. Nanda, P.C. Stair, J.M. Notestein, Tandem In_2O_3-Pt/Al_2O_3 catalyst for coupling of propane dehydrogenation to selective H_2 combustion, Science 371 (2021) 1257–1260.
[47] J. Li, Q. Guan, H. Wu, W. Liu, Y. Lin, Z. Sun, X. Ye, X. Zheng, H. Pan, J. Zhu, S. Chen, W. Zhang, S. Wei, J. Lu, Highly active and stable metal single-atom catalysts achieved by strong electronic metal-support interactions, J. Am. Chem. Soc. 141 (2019) 14515–14519.
[48] J. Gan, J. Zhang, B. Zhang, W. Chen, D. Niu, Y. Qin, X. Duan, X. Zhou, Active sites engineering of Pt/CNT oxygen reduction catalysts by atomic layer deposition, J. Energy Chem. 45 (2020) 59–66.
[49] J. Zhang, Z. Yu, Z. Gao, H. Ge, S. Zhao, C. Chen, S. Chen, X. Tong, M. Wang, Z. Zheng, Y. Qin, Porous TiO_2 nanotubes with spatially separated platinum and CoO_x cocatalysts produced by atomic layer deposition for photocatalytic hydrogen, Angew. Chem. Int. Ed. 56 (2017) 816–820.
[50] Y. Qin, Z. Zhang, Z. Cui, Helical carbon nanofibers prepared by pyrolysis of acetylene with a catalyst derived from the decomposition of copper tartrate, Carbon 41 (2003) 3072–3074.
[51] S. Li, Y. Xu, Y. Chen, W. Li, L. Lin, M. Li, Y. Deng, X. Wang, B. Ge, C. Yang, S. Yao, J. Xie, Y. Li, X. Liu, D. Ma, Tuning the selectivity of catalytic carbon dioxide hydrogenation over iridium/cerium oxide catalysts with a strong metal-support interaction, Angew. Chem. Int. Ed. 129 (2017) 10901–10905.
[52] C. Rivera-Cárcamo, I.C. Gerber, I. del Rosal, B. Guicheret, R.C. Contreras, L. Vanoye, A. Favre-Réguillon, B.F. Machado, J. Audevard, C. de Bellefon, R. Philippe, P. Serp, Control of the single atom/nanoparticle ratio in Pd/C catalysts to optimize the cooperative hydrogenation of alkenes, Catal. Sci. Technol. 11 (2021) 984–999.
[53] P. Verma, K. Yuan, Y. Kuwahara, K. Mori, H. Yamashita, Enhancement of plasmonic activity by Pt/Ag bimetallic nanocatalyst supported on mesoporous silica in the hydrogen production from hydrogen storage material, Appl. Catal. B Environ. 223 (2018) 10–15.
[54] W.-W. Zhan, Q.-L. Zhu, Q. Xu, Dehydrogenation of ammonia borane by metal nanoparticle catalysts, ACS Catal. 6 (2016) 6892–6905.
[55] L. Wang, H. Li, W. Zhang, X. Zhao, J. Qiu, A. Li, X. Zheng, Z. Hu, R. Si, J. Zeng, Supported rhodium catalysts for ammonia-borane hydrolysis: dependence of the catalytic activity on the highest occupied state of the single rhodium atoms, Angew. Chem. Int. Ed. 56 (2017) 4712–4718.
[56] F. Fu, C. Wang, Q. Wang, A. Martinez-Villacorta, A. Escobar, H. Chong, X. Wang, S. Moya, L. Salmon, E. Fouquet, J. Ruiz, D. Astruc, Highly selective and sharp volcano-type synergistic Ni_2Pt@ZIF-8-catalyzed hydrogen evolution from ammonia borane hydrolysis, J. Am. Chem. Soc. 140 (2018) 10034–10042.
[57] W. Wang, Z.H. Lu, Y. Luo, A. Zou, Q. Yao, X. Chen, Mesoporous carbon nitride supported Pd and Pd-Ni nanoparticles as highly efficient catalyst for catalytic hydrolysis of NH_3BH_3, ChemCatChem 10 (2018) 1620–1626.
[58] J. Manna, S. Akbayrak, S. Özkar, Palladium(0) nanoparticles supported on polydopamine coated $CoFe_2O_4$ as highly active, magnetically isolable and reusable catalyst for hydrogen generation from the hydrolysis of ammonia borane, Appl. Catal. B Environ. 208 (2017) 104–115.
[59] C. Mboyi, D. Poinsot, J. Roger, K. Fajerwerg, M. Kahn, J.-C. Hierso, The hydrogen-storage challenge: Nanoparticles for metal-catalyzed ammonia borane dehydrogenation, Small 17 (2021), 2102759.
[60] X. Huang, Y. Liu, H. Wen, R. Shen, S. Mehdi, X. Wu, E. Liang, X. Guo, B. Li, Ensemble-boosting effect of Ru-Cu alloy on catalytic activity towards hydrogen evolution in ammonia borane hydrolysis, Appl. Catal. B Environ. 287 (2021), 119960.
[61] P. Li, R. Chen, S. Zhao, W. Li, Y. Lin, Y. Yu, Architecture control and electronic structure engineering over Ni-based nitride nanocomposite for boosting ammonia borane dehydrogenation, Appl. Catal. B Environ. 298 (2021), 120523.
[62] W. Chen, D. Li, C. Peng, G. Qian, X. Duan, D. Chen, X. Zhou, Mechanistic and kinetic insights into the Pt-Ru synergy during hydrogen generation from ammonia borane over PtRu/CNT nanocatalysts, J. Catal. 356 (2017) 186–196.
[63] Z. Li, T. He, D. Matsumura, S. Miao, A. Wu, L. Liu, G. Wu, P. Chen, Atomically dispersed Pt on the surface of Ni particles: synthesis and catalytic function in hydrogen generation from aqueous ammonia-borane, ACS Catal. 7 (2017) 6762–6769.
[64] Z. Gao, M. Dong, G. Wang, P. Sheng, Z. Wu, H. Yang, B. Zhang, G. Wang, J. Wang, Y. Qin, Multiply confined nickel nanocatalysts produced by atomic layer deposition for hydrogenation reactions, Angew. Chem. Int. Ed. 54 (2015) 9006–9010.
[65] P.C. Stair, Where the action is, Nat. Chem. 3 (2011) 345.
[66] C. Dong, Y. Li, D. Cheng, M. Zhang, J. Liu, Y.-G. Wang, D. Xiao, D. Ma, Supported metal clusters: Fabrication and application in heterogeneous catalysis, ACS Catal. 10 (2020) 11011–11045.